Time-frequency resolved analysis of a nanosecond supercontinuum source dedicated to multiplex CARS application

Annalisa De Angelis,[1] Alexis Labruyère,[1,*] Vincent Couderc,[1] Philippe Leproux,[1] Alessandro Tonello,[1] Hiroki Segawa,[2] Masanari Okuno,[2] Hideaki Kano,[2,3] Delia Arnaud-Cormos,[1] Philippe Lévèque,[1] and Hiro-o Hamaguchi[2,4]

[1] *Xlim Institute, UMR CNRS 7252, 123 avenue Albert Thomas, 87060 Limoges cedex, France*
[2] *Department of Chemistry, School of Science, The University of Tokyo, Hongo 7-3-1, Bunkyo, Tokyo 113-0033, Japan*
[3] *Currently with the Institute of Applied Physics, University of Tsukuba, 1-1-1, Tennodai, Tsukuba, Ibaraki 305-8573, Japan*
[4] *Institute of Molecular Science and Department of Applied Chemistry, National Chiao Tung University, Ta Hsueh Road 1001, Hsinchu 300, Taiwan*
[*] *alexis.labruyere@xlim.fr*

Abstract: In this paper, we describe and investigate the properties of a broadband source designed from a nanosecond microchip laser operating at high repetition rate and dedicated to multiplex-CARS application. We demonstrate that a strong reshaping of the initial pulse profile drastically affects the Stokes wave and therefore represents an important limitation in CARS experiment. In particular, we emphasize the saturation effect of the peak power of the Stokes wave resulting from supercontinuum generation. However, we show that this type of compact system can be particularly suitable for achieving CARS measurement.

OCIS codes: (190.4370) Nonlinear optics, fibers; (180.5655) Raman microscopy.

References and links

1. K. Kneipp, H. Kneipp, I. Itzkan, R. R. Dasari, and M. S. Feld, "Ultrasensitive chemical analysis by Raman spectroscopy," Chem. Rev. **99**, 2957–2976 (1999).
2. O. Samek, H. H. Telle, L. G. Harris, M. Bloomfield, and D. Mack, "Raman spectroscopy for rapid discrimination of Staphylococcus epidermidis clones related to medical device-associated infections," Laser Phys. Lett. **5**, 465–470 (2008).
3. I. Nabiev, I. Chourpa, and M. Manfait, "Applications of Raman and surface-enhanced Raman scattering spectroscopy in medicine," J. Raman Spectrosc. **25**, 13–23 (1994).
4. W. Werncke, I. Latka, S. Sassning, B. Dietzek, M. E. Darvin, M. C. Meinke, J. Popp, K. König, J. W. Fluhr, and J. Lademann, "Two-color Raman spectroscopy for the simultaneous detection of chemotherapeutics and antioxidative status of human skin," Laser Phys. Lett. **8**, 895–900 (2011).
5. M. Okuno, H. Kano, P. Leproux, V. Couderc, J. P. R. Day, M. Bonn, and H. Hamaguchi, "Quantitative CARS molecular fingerprinting of single living cells with the use of the maximum entropy method," Angew. Chem **49**, 6773–6777 (2010).
6. J.-X. Cheng, Y. K. Jia, G. Zheng, and X. S. Xie, "Laser-scanning coherent anti-Stokes Raman scattering microscopy and applications to cell biology," Biophys. J. **83**, 502–509 (2002).
7. E. E. Serebryannikov, and A. M. Zheltikov, "Supercontinuum generation through cascaded four-wave mixing in photonic-crystal fibers: When picoseconds do it better," Opt. Commun. **274**, 433–440 (2007).
8. S. Gao, X. Li, and S. Zhang, "Supercontinuum generation by combining clad-pumped Er/Yb co-doped fiber amplifier and highly nonlinear photonic crystal fiber," Optik **121**, 2110–2112 (2010).

#178746 - $15.00 USD Received 6 Nov 2012; revised 30 Nov 2012; accepted 30 Nov 2012; published 20 Dec 2012

9. J. X. Cheng, and T. B. Huff, "In vivo coherent anti-Stokes Raman scattering imaging of sciatic nerve tissue," J. Microsc. **225**, 175–182 (2007).
10. K. König, H. G. Breunig, R. Bückle, M. Kellner-Höfer, M. Weinigel, E. Büttner, W. Sterry, and J. Lademann, "Optical skin biopsies by clinical CARS and multiphoton fluorescence/SHG tomography," Laser Phys. Lett. **8**, 465–468 (2011).
11. T. W. Kee, and M. T. Cicerone, "Simple approach to one-laser, broadband coherent anti-Stokes Raman scattering microscopy," Opt. Lett. **29**, 2701–2703 (2004).
12. H. Kano, and H. Hamaguchi, "Dispersion-compensated supercontinuum generation for ultrabroadband multiplex coherent anti-Stokes Raman scattering spectroscopy," J. Raman Spectrosc. **37**, 411–415 (2006).
13. J. X. Cheng, and X. S. Xie, "Coherent anti-Stokes Raman scattering microscopy: instrumentation, theory and application," J. Phys. Chem. **108**, 827–840 (2004).
14. G. Bergner, D. Akimov, S. Schlücker, H. Bartelt, B. Dietzek, and J. Popp, "Tunable optical setup with high flexibility for spectrally resolved coherent anti-Stokes Raman scattering microscopy," Laser Phys. Lett. **8**, 541–546 (2011).
15. A. Zumbusch, G. R. Holtom, and X. S. Xie, "Three-dimensional vibrational imaging by coherent anti-Stokes Raman scattering," Phys. Rev. Lett. **82**, 4142–4145 (1999).
16. M. Hashimoto, T. Araki, and S. Kawata, "Molecular vibration imaging in the fingerprint region by use of coherent anti-Stokes Raman scattering microscopy with collinear configuration," Opt. Lett. **25**, 1768–1770 (2000).
17. E. O. Potma, D. J. Jones, J.-X. Cheng, X. S. Xie, and J. Ye, "High-sensitivity coherent anti-Stokes Raman scattering microscopy with two tightly synchronized picosecond lasers," Opt. Lett. **27**, 1168–1170 (2002).
18. C. L. Evans, E. O. Potma, M. Puoris'haag, D. Coté, C. P. Lin, and X. S. Xie, "Chemical imaging of tissue in vivo with video-rate coherent anti-Stokes Raman scattering microscopy," Proc. Natl. Acad. Sci. USA **102**, 16807 (2005).
19. H. N. Paulsen, K. M. Hilligsoe, J. Thogersen, S. R. Keiding, and J. J. Larsen, "Coherent anti-Stokes Raman scattering microscopy with a photonic crystal fiber based light source," Opt. Lett. **28**, 1123–1125 (2003).
20. H. Kano, and H. Hamaguchi, "Vibrationally resonant imaging of a single living cell by supercontinuum-based multiplex coherent anti-Stokes Raman scattering microspectroscopy," Opt. Express **13**, 1322–1327 (2005).
21. V. P. Mitrokhin, A. B. Fedotov, A. A. Ivanov, M. V. Alfimov, and A. M. Zheltikov, "Coherent anti-Stokes Raman scattering microspectroscopy of silicon components with a photonic-crystal fiber frequency shifter," Opt. Lett. **32**, 3471–3473 (2007).
22. F. Ganikhanov, S. Carrasco, X. S. Xie, M. Katz, W. Seitz, and D. Kopf, "Broadly tunable dual-wavelength light source for coherent anti-stokes Raman scattering microscopy," Opt. Lett. **31**, 1292–1294 (2006).
23. M. Okuno, H. Kano, P. Leproux, V. Couderc, and H. Hamaguchi, "Ultrabroadband (>2000 cm^{-1}) multiplex coherent anti-Stokes Raman scattering spectroscopy using a subnanosecond supercontinuum light source," Opt. Lett. **32**, 3050–3052 (2007).
24. M. Okuno, H. Kano, P. Leproux, V. Couderc, and H. Hamaguchi, "Ultrabroadband multiplex CARS microspectroscopy and imaging using a subnanosecond supercontinuum light source in the deep near infrared," Opt. Lett. **33**, 923–925 (2008).
25. J. Cheng, A. Volkmer, L. D. Book, and X. S. Xie, "An epi-detected coherent anti-Stokes Raman scattering (E-CARS) microscope with high spectral resolution and high sensitivity," J. Phys. Chem. B **105**, 1277–1280 (2001).
26. J. M. Dudley, G. Genty, and B. J. Eggleton, "Harnessing and control of optical rogue waves in supercontinuum generation," Opt. Express **16**, 3644–3651 (2008).
27. D. R. Herriott, and H. J. Schulte, "Folded optical delay lines," Appl. Opt. **4**, 883–889 (1965).
28. G. P. Agrawal, P. L. Baldeck, and R. R. Alfano, "Modulation instability induced by cross-phase modulation in optical fibers," Phys. Rev. A **39**, 3406–3413 (1989).

1. Introduction

Raman scattering is a nonlinear effect discovered in 1927, in which photons are scattered by molecules inelastically, thus scattered photons having a frequency detuned from that of incident photons. It has important practical applications in biology and medicine [1–4]. In particular, coherent anti-Stokes Raman scattering (CARS) offers the possibility of imaging molecules in biological media at the microscopic scale with relatively high spatial resolution and in a way that is essentially noninvasive for the living matter [5–8]. The principle of CARS is based on the excitation of the vibration of the molecule that is coherently driven by two incident lasers, whose frequencies are usually referred to as the "pump" and the "Stokes" waves and denoted as ω_p and $\omega_s < \omega_p$, respectively. It eventually yields the emission of a CARS signal, i.e. an anti-Stokes wave at the frequency $\omega_{as} = 2\omega_p - \omega_s$. Whenever the pump detuning $\omega_p - \omega_s$ is resonant with the vibration, the CARS signal is significantly enhanced and thus the presence of

#178746 - $15.00 USD Received 6 Nov 2012; revised 30 Nov 2012; accepted 30 Nov 2012; published 20 Dec 2012

the molecule is detected [9, 10]. The coherent process of CARS interaction is advantageously much more efficient in comparison with the usual Raman scattering process since the vibration of the molecule under investigation is forced by the frequency detuning between the pump and the Stokes waves. The biological medium is typically composed by an ensemble of molecules whose vibration can be probed by CARS. In this context, the use of polychromatic light is required for investigating different molecules simultaneously. To that end, a particular attention has been paid to the multiplex CARS technique, which enables to probe several chemical bonds simultaneously by using the combination of a monochromatic pump and a broadband spectrum of light, thus playing the role of Stokes components [11, 12].

The development of laser sources has been essential for the advent of CARS microscopy [13, 14]. Indeed, laser sources have evolved from low-repetition-rate femtosecond amplified systems [15,16], to electronically synchronized picosecond sources of MHz repetition-rate [17] or to synchronously-pumped optical parametric oscillator (OPO) systems [18]. Additionally, supercontinuum (SC) sources have been achieved by the use of a femtosecond oscillator coupled with a mm-long photonic crystal fibre (PCF) [11, 19–21], or with a mm-long tapered nonlinear fibre [11]. Thanks to the use of PCFs, the need for too much sophisticated laser systems, i.e., cavity dumped oscillators or two synchronized oscillators [17,22], can be avoided. Because of their high nonlinearity and highly-tunable dispersion properties [23,24], these fibres provide a unique medium for nonlinear interaction and particularly for generating the broadband signal used as Stokes waves in multiplex CARS experiments.

Femtosecond lasers provide the high peak-power required for optical nonlinear effects and SC generation. Hence, a broadband Stokes wave could be easily obtained from propagation of femtosecond pulses in nonlinear PCFs. However, the power spectrum of SC generated from femtosecond pump pulses is usually fluctuating across the infrared because the pump energy aggregates in the form of solitons at different locations in the spectrum. Additionally, because of the very short pulse duration, each created soliton propagates in the PCF with its own group velocity and walks off very quickly, therefore leading to a very large temporal spreading out of the output polychromatic Stokes wavelengths. Further re-synchronization between the pump and all the components of the polychromatic Stokes wave is then dramatically difficult in practice. Moreover, spectral filtering of the initial femtosecond pump pulse has to be achieved to improve the spectral resolution of the CARS process [16].

A very promising alternative to the femtosecond or picosecond lasers is provided by the microchip lasers. Those are miniature light sources capable to deliver subnanosecond pulses which broaden into a very large and relatively flat spectrum of light when used in combination with PCFs [5, 23, 24]. This type of ultracompact system offers a high spectral resolution because of its Fourier-transformed subnanosecond pump pulses and allows to probe simultaneously a large variety of chemical bonds thanks to a better temporal synchronisation of all the wavelengths contained in the Stokes wave. Therefore, the recording of multicoloured images by the CARS technique is simplified [25]. Nevertheless, there is still a lack of synchronization between the Stokes components in the nanosecond regime which, although reduced when compared to the femtosecond regime, is more complicated to explain [20]. Indeed, the interplay between several nonlinear effects yields large temporal instabilities including the build-up of optical solitons and rogue waves propagating in presence of large Raman perturbation which drastically distorts the overall envelop of the signal [26].

In this paper, we perform a time-frequency analysis of a nanosecond SC source dedicated to CARS experiments. We emphasize the large distortions undergone by nanosecond pulses when propagating in a nonlinear PCF and we point out several impairments related to those distortions which have not been adressed before, such as the nonlinear temporal broadening and saturable transparency effect, thus limiting the efficiency of the CARS process. We demon-

#178746 - $15.00 USD Received 6 Nov 2012; revised 30 Nov 2012; accepted 30 Nov 2012; published 20 Dec 2012

strate the important role played by the stimulated Raman scattering in the emergence of the infrared SC and its interplay with competing nonlinear effects such as modulation instability and solitons. Temporal superimposition between coherent subnanosecond pump pulse and incoherent SC Stokes waves used for multiplex-CARS is investigated in the near infrared (NIR) domain.

2. Experimental setup

A schematic representation of the dual-output compact laser source used in this work is shown in Fig. 1. The pump source is a passively Q-switched microchip laser which is longitudinally single-mode and delivers subnanosecond (950 ps FWHMI) pulses at 1064 nm with a repetition rate of 75 kHz [see Figs. 2(a) and 2(c)]. The laser beam is divided in two parts whose ratio of energy can be adjusted by using a half-wave plate and a beam splitter. One part is directly used as a pump wave (average power: 200 mW, peak power: 2.7 kW) in the CARS process after passing through a Herriott-type delay-line for synchronizing the pump and the Stokes pulses. The latter is a peculiar type of multi-pass delay line which consists of two curved mirrors separated by a suitable distance such that a stable configuration is obtained for the resonator [27]. A fixed insertion mirror (not shown in the schematic setup) is placed off-axis near one of the mirrors, and a mobile mirror is placed inside the cavity in order to extract the beam. When the Herriott cavity parameters are properly adjusted, the incident beam injected with the appropriate offset and tilt undergoes a large number of reflections and thus, travels a long optical path in the small volume of the cavity. The other part of the laser beam is used as a Stokes wave after amplification in an ytterbium-doped fiber amplifier (YDFA) and SC generation by propagation into a 7-m-long air-silica PCF. The YDFA consists of a 6-m-long double-clad fiber exhibiting a single transverse mode at 1064 nm and having a zero-dispersion wavelength (ZDW) at 1.3 μm. The available average power at the amplifier output is 900 mW which corresponds to more than 12.5 kW equivalent peak power. Monochromatic and polychromatic beams are spatially super-

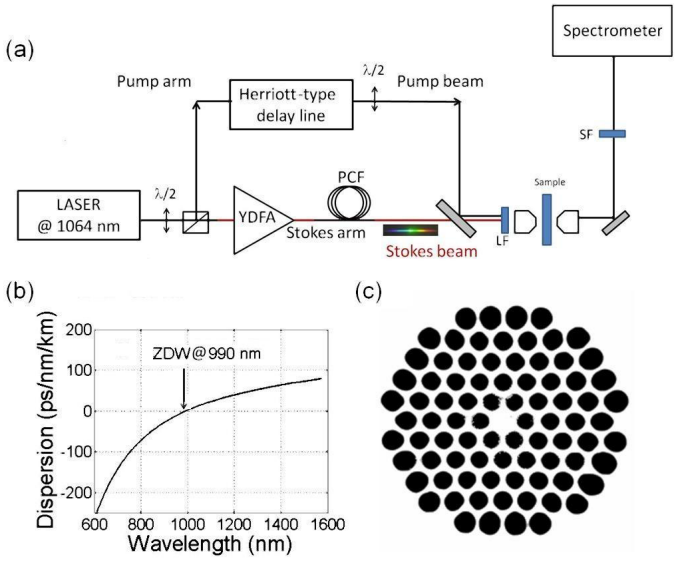

Fig. 1. (a) Schematic representation of the dual-output light source designed for multiplex-CARS microspectroscopy applications; (b) dispersion curve for the fundamental guided mode of the PCF used in our experiment (ZDW $\simeq$ 990 nm), and (c) air holes distribution in the section of the PCF.

#178746 - $15.00 USD Received 6 Nov 2012; revised 30 Nov 2012; accepted 30 Nov 2012; published 20 Dec 2012

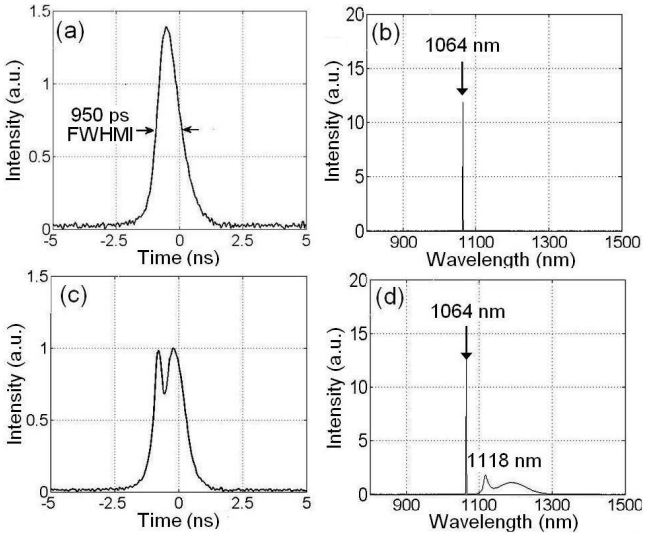

Fig. 2. (a) and (b) pulse and spectral profiles before amplification in the YDFA, respectively; (c) pulse profile at 1064 nm at the entrance of PCF after amplification in the YDFA; (d) spectral profile at the entrance of PCF after amplification in the YDFA.

imposed by means of a dichroic plate before reaching the microscope stage. The core diameter of the PCF is 4.2 μm while the hole diameter and the hole-to-hole spacing are 2.5 μm and 4 μm respectively [see Fig. 1(c)]. The dispersion curve of the PCF represented in Fig. 1(b) was obtained using a mode-solver. The calculated ZDW is 990 nm for the fundamental mode. The strong third-order nonlinear effects occurring all along the propagation in the PCF generate a polychromatic radiation at the output. A part of this continuum beam (from 1 μm to 2.4 μm) is used as the Stokes wave of the CARS process. The two beams are sent in a microscope through a long pass filter (LF) and the CARS signal is recorded with a spectrometer through a short pass filter (SP).

3. Results and discussion

The temporal and spectral characteristics of the beam produced by the microchip laser are shown in Figs. 2(a) and 2(b) respectively (pulse width: 950 ps FWHMI, spectrum width: $\simeq$2 pm). The pulse profiles represented in Figs. 2(a) and 2(c) are measured using a 10-GHz photodiode connected to a 16-GHz oscilloscope. After propagation in the YDFA, a powerful beam (average power: 900 mW) exhibiting minor spectral and temporal distortions is obtained. During propagation in the YDFA, Raman conversion partially depletes the central part of the pulse and produces a frequency conversion toward infrared domain [see Figs. 2(c) and 2(d)]. The Raman conversion efficiency was determined by subtracting the integrals of the temporal profiles represented in Figs. 2(c) and 2(a), then dividing the obtained quantity by the integral of the temporal profile in Fig. 2(a). It is estimated to be only 10% of the initial energy but is sufficient to induce a significant modification of the temporal shape with the emergence of a depletion in the central part of the nanosecond pulse. After propagation in the PCF, a SC is obtained in the infrared domain between 1064 nm and 2200 nm (see Fig. 3). The interplay between self-phase modulation and dispersion yields in the early stage of propagation in the PCF to a self-induced instability, referred to as modulation instability (MI) that occurs in the anomalous dispersion regime and leads to the break-up of the initial nanosecond pulse into a

#178746 - $15.00 USD Received 6 Nov 2012; revised 30 Nov 2012; accepted 30 Nov 2012; published 20 Dec 2012

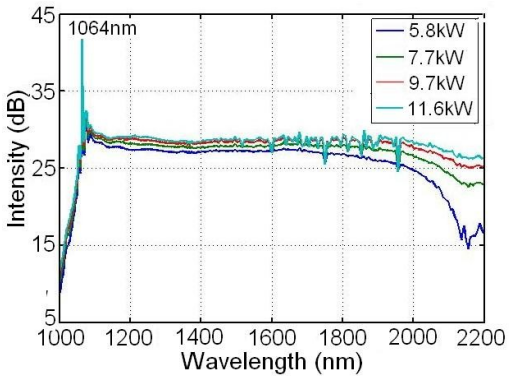

Fig. 3. Power spectrum of the Stokes beam obtained by SC generation in the PCF for four different values of the peak power measured at the entrance of the PCF.

train of ultrashort solitons [28]. The spectral broadening towards infrared wavelengths is subsequently driven by Raman soliton self-frequency shift enhanced by compression throughout soliton collisions in the presence of Raman gain. At the output end of the PCF, an incoherent infrared beam composed with a large number of ultrashort pulses is generated. The spectrum is particularly flat with an overall amplitude difference lower than 5 dB over the entire infrared domain between 1 μm and 2.2 μm (Fig. 3). This spectral profile is recorded by means of an optical spectrum analyser and results from averaging over a large number of shots ($>$10).

Unless specified, the peak power will be fixed throughout this paper to the value of 11.6 kW which corresponds to the maximum peak power used in Fig. 3.

At this stage, no information is obtained on the temporal distribution of the continuum energy that is however of major importance for multiplex CARS applications. Therefore, we recorded the spectrogram of the SC radiation both in the time domain and in the frequency domain. The experimental setup used to measure spectrograms is shown in Fig. 4. The laser source, the fiber amplifier (YDFA) and the PCF represented here are those described in section 2, respectively. The laser beam is first divided in two parts using a beam splitter (BS1). One part is directly detected using a 10-GHz photodiode (pd1) connected to a 16-GHz oscilloscope, thus playing the role of a reference signal for triggering the oscilloscope. The other part of the laser beam is injected in the YDFA fiber, and then propagates in the PCF so as to generate the broadband SC light. The spectral components of the SC spectrum are separated using a diffraction grating, then selected individually using a pinhole and detected both with a spectrum analyser (to measure the selected wavelength) and a 10-GHz photodiode (pd2) connected to the oscilloscope. The temporal and spectral resolutions are 20 ps and 30 nm, respectively. The recorded data are then assembled together to form a spectrogram.

Figure 5(a) represents the spectrogram of the SC recorded at the output end of the PCF showing that the central part of the pump pulse at 1064 nm is fully depleted at the output of the PCF.

Indeed, stimulated Raman scattering is the dominant effect during propagation in the PCF and is tranferring all the energy contained in the central part of the pump pulse towards infrared wavelengths while the tails whose intensity is below the Raman threshold remain undepleted. Hence, the output profile of the pump pulse is dramatically transformed from a 950-ps almost gaussian shape [see Fig. 2(c)] into two shorter pulses formed by the remaining tails and delayed by more than 2 ns [see Fig. 5(b) at 1065 nm]. Similar distortion can be observed in Fig. 5(b) for longer wavelengths above 1064 nm as the different profiles shown Fig. 5(b) exhibit as well

#178746 - $15.00 USD Received 6 Nov 2012; revised 30 Nov 2012; accepted 30 Nov 2012; published 20 Dec 2012

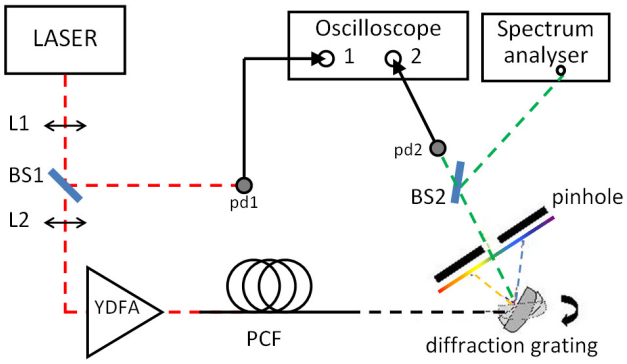

Fig. 4. Experimental setup used to measure the spectrograms. (L1)-(L2): convergent lenses; (BS1)-(BS2): beam splitters; (pd1)-(pd2): photodiodes.

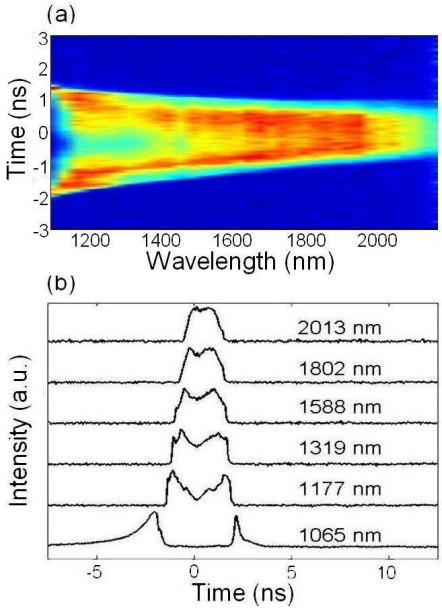

Fig. 5. (a) Spectrogram of the SC recorded at the output end of the PCF obtained for a peak power of 11.6 kW. (b) Different pulse profiles obtained at the wavelengths of 2013 nm, 1802 nm, 1588 nm, 1319 nm, 1177 nm and 1065 nm, respectively.

some power depletion in the central part which tends to disappear for the longer wavelengths. This Raman-induced depletion acts as a pulse reshaping effect for infrared wavelengths. It is worth noticing that the undepleted tails of the pulse which do not undergo the Raman gain are affected by MI, solitonic propagation and soliton self-frequency shift (SSFS). Hence they form two time-separated continua extending up to 1.3 μm. Then from 1.3 μm to 2.2 μm, the gap between these two continua is gradually filled by all the energy initially contained in the central part of the pump pulse and in the first-order Stokes which is redistributed via MI and solitonic collisions.

At this stage, we would like to emphasize the following important point. In practice, it is rather unusual when a quasi-CW or nanosecond pulse propagates in the anomalous dispersion

#178746 - $15.00 USD Received 6 Nov 2012; revised 30 Nov 2012; accepted 30 Nov 2012; published 20 Dec 2012

domain, that Raman effect dominates in the early stage of propagation. MI usually occurs first whereas Raman scattering arises later on during propagation and essentially manifests via the SSFS in general. The unusual behaviour that we observe here can be easily understood by noticing that the Raman-induced Stokes generation is initiated earlier when propagating in the YDFA. Because of strong amplification, the central part of the 1064 nm pulse propagating in normal dispersive regime in the YDFA eventually exceeds the Raman threshold and therefore experiences Raman effect. That results in initiating the depletion of the central part of the pulse to form the first Stokes peak at 1118 nm [see Fig. 2(d)]. The coupling of these two radiations in the PCF (pump and first Raman Stokes radiations) acts as an optical seeding that decreases the Raman threshold. Therefore, Raman effect occurs first in the PCF and is responsible for the strong depletion of the initial pulse. The onset phase of MI generally observed in the very first stage of propagation in the anomalous dispersion regime arises later and is clearly visible for wavelengths above 1500 nm. In contrast, because of their reduced power, the tails of the pulse are not affected by the Raman gain but rather by MI, soliton collisions and SSFS, thus producing a continuous spectral broadening.

Hence, because of initial pump conditions set at the input PCF, the threshold of Raman effect is lower than that of MI and therefore priorly affects the pulse spectrum. This competition between MI and Raman Stokes conversion can be illustrated by the following approximate calculation. Roughly speaking, the spectral density of power Γ at the frequency Ω_{MI} where the MI gain is maximum can be evaluated as:

$$\Gamma(\Omega_{\mathrm{MI}}) \quad = \quad \Gamma_{\mathrm{noise}}\, \mathrm{e}^{2\gamma P_0 z}, \tag{1}$$

where z is the propagation distance, P_0 represents the quasi-CW pump power, Γ_{noise} is the average spectral density of noise, and γ is the nonlinear coefficient of the fiber. For comparison, the maximum spectral density of power at the frequency Ω_{max} $\sim$13.2 THz where the Raman gain is maximum is

$$\Gamma(\Omega_{\mathrm{max}}) \quad = \quad \Gamma_{\mathrm{noise}}\, \mathrm{e}^{\delta + g_{\mathrm{R}} P_0 z}, \tag{2}$$

where δ is an additional gain factor accounting for prior amplification of the noise in the YDFA, and $g_{\mathrm{R}} = 2\gamma f_{\mathrm{R}} \mathrm{Im}[\chi_{\mathrm{R}}(\Omega_{\mathrm{max}})]$ is the Raman gain coefficient with $f_{\mathrm{R}} \sim 0.18$ and $\mathrm{Im}[\chi_{\mathrm{R}}(\Omega_{\mathrm{max}})] \sim 1.39$ in silica glass. One can define some characteristic lengths for MI or Raman Stokes conversion as the lengths of propagation after which the spectral density of power exceeds an arbitrary value of reference Γ_{ref}, respectively. Hence, the characteristic length for MI reads as

$$L_{\mathrm{MI}} \quad = \quad \frac{1}{2\gamma P_0} \log\left(\Gamma_{\mathrm{ref}}/\Gamma_{\mathrm{noise}}\right), \tag{3}$$

and the characteristic length for Raman effect is given by

$$L_{\mathrm{R}} \quad = \quad \frac{1}{g_{\mathrm{R}} P_0} \left[\log\left(\Gamma_{\mathrm{ref}}/\Gamma_{\mathrm{noise}}\right) - \delta\right]. \tag{4}$$

In the above formulae, Γ_{ref} is an arbitrary level of power above which one consider that a sideband emerging from noise can be detected. Let us now consider the three different situations depicted in Fig. 6, namely (i) when MI reaches the power of reference first which is the usual situation in SC generation without amplification of the pump pulse, (ii) when MI and Raman reach Γ_{ref} at the same distance, and (iii) when Raman reaches this threshold first as typically in the situation where the pump pulse is amplified in the YDFA fiber. In case that $\delta = 0$, then $L_{\mathrm{R}} \sim 4L_{\mathrm{MI}}$, and hence the early stage of propagation is dominated by MI. In contrast, if $\delta > 0$,

#178746 - $15.00 USD Received 6 Nov 2012; revised 30 Nov 2012; accepted 30 Nov 2012; published 20 Dec 2012

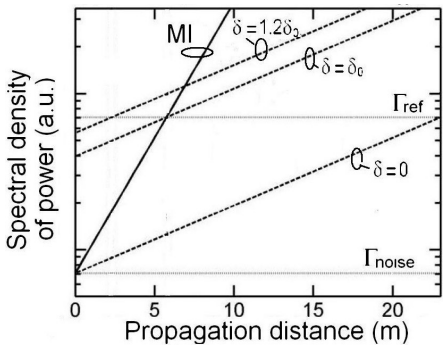

Fig. 6. Spectral density of power vs. propagation distance z, for $\gamma = 0.02$ m^{-1}W^{-1} and P_0 = 10 W. Dotted lines stand for Γ_{noise} and $\Gamma_{\text{ref}} = 10\Gamma_{\text{noise}}$, respectively. Solid line stands for the evolution of the maximum spectral power density of MI sidebands. The dashed lines indicate the maximum spectral power density of the Raman peak for the different cases when $\delta = 0$, $\delta = \delta_0$, and $\delta = 1.2\delta_0$, respectively.

the Raman length is decreased and eventually equals the MI length if $\delta \equiv \delta_0$, where

$$\begin{aligned} \delta_0 &= \left[1 - \frac{g_{\text{R}}}{2\gamma}\right] \log\left(\Gamma_{\text{ref}}/\Gamma_{\text{noise}}\right) \\ &= \{1 - f_R \text{Im}[\chi_R(\Omega_{\max})]\} \log\left(\Gamma_{\text{ref}}/\Gamma_{\text{noise}}\right). \end{aligned} \tag{5}$$

However, if $\delta > \delta_0$, the Raman length will be shorter than the MI length and hence, the Raman effect acts before the emergence of MI sidebands. For example, if we consider a reference spectral density of power that is 10 dB above that of the noise, then $\delta_0 \sim 1.726$ (see Fig. 6).

Whereas Raman gain is the dominant effect in the early stage of propagation, both nonlinear effects (Raman and MI) subsequently contribute to the spectral broadening and remain in competition throughout propagation. Indeed, after few meters of propagation, MI progressively enters into play and ultimately breaks up the pulse structure into a periodic train of solitons. The MI signature is clearly visible for wavelengths longer than 1.55 μm. At this stage, soliton propagation and SSFS dominate as the Raman scattering essentially manifests via the SSFS and not via the Stokes generation. The output pulse envelop obtained for wavelengths above 1600 nm, exhibits square shape with enclosed femtosecond pulses. The envelop durations at these wavelengths are much larger than that of the initial pump pulse at 1064 nm and progressively decrease as the wavelength increase. This temporal evolution is induced by the initial gaussian pulse profile where the conversion toward longer wavelengths is produced by the most powerful part of the pulse.

In order to illustrate the situation when MI dominates in the early stage of SC generation over the stimulated Raman scattering, we achieved SC generation in the PCF while removing the prior stage of amplification in the YDFA fiber. In this situation, subnanosecond laser pulses represented in Fig. 2(b) are directly injected in the PCF. The peak power of the laser pulses is fixed to 11.6 kW as in the previous experiment, but the repetition rate is only 10 kHz, resulting in a lower average pump power. The spectro-temporal evolution of the Stokes wave at the output of the PCF is represented in Fig. 7(a). It was measured using the setup represented in Fig. 4. The first nonlinear effect occuring during the propagation is MI followed by soliton dynamics. Hence, the envelop of the initial pulse is periodically modulated and ultimately transformed into a periodic train of solitons which later on collide and exchange energy throughout propagation. Lower depletion of the pulse center is obtained when compared to Fig. 5(a). The output pulse

#178746 - $15.00 USD Received 6 Nov 2012; revised 30 Nov 2012; accepted 30 Nov 2012; published 20 Dec 2012

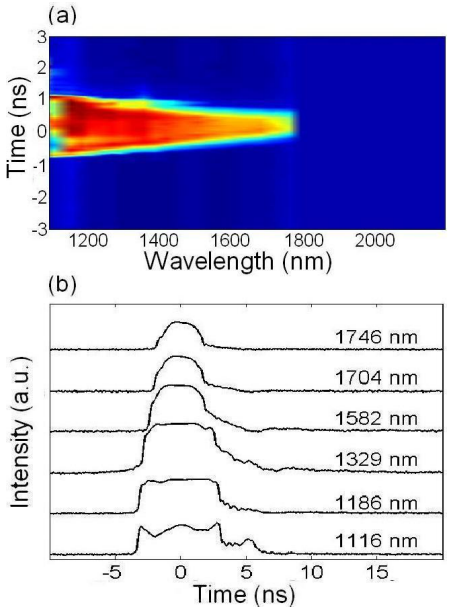

Fig. 7. (a) Spectrogram of the SC recorded at the output end of the PCF. (b) Different pulse profiles obtained at the wavelengths of 1746 nm, 1704 nm, 1582 nm, 1329 nm, 1186 nm and 1116 nm, respectively.

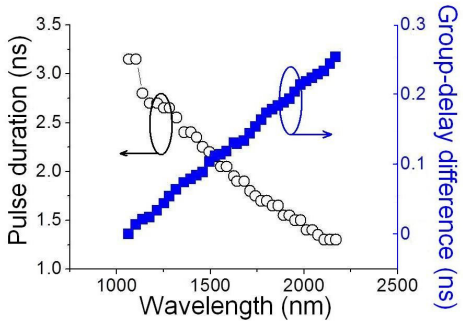

Fig. 8. Stokes pulses duration (circles) and group-delay difference (squares) vs. wavelength.

envelops exhibit quasi-square shapes significantly larger than the initial pulse duration [see Fig. 7(b)].

Moreover, because of the short fiber length (7 m) used in the experiment, a weak influence of the group velocity difference is observed on the spectro-temporal profile [see Fig. 5(b)]. The infrared pulses propagate slower than the other ones in the anomalous dispersion regime, and are progressively delayed all along the propagation in the fiber. The maximum delay obtained at the output end of the fiber is estimated to 254 ps (see Fig. 8, square dots). By this way the fall time of all the pulses at each wavelength are practically synchronized [see Fig.9(b)]. The maximum pulse broadening observed on the spectro-temporal representation is obtained for wavelengths close to the pump and reaches 3 ns (FWHMI). The minimum pulse duration is obtained for infrared pulses above 2 μm and reaches 1.3 ns (see Fig.8).

#178746 - $15.00 USD Received 6 Nov 2012; revised 30 Nov 2012; accepted 30 Nov 2012; published 20 Dec 2012

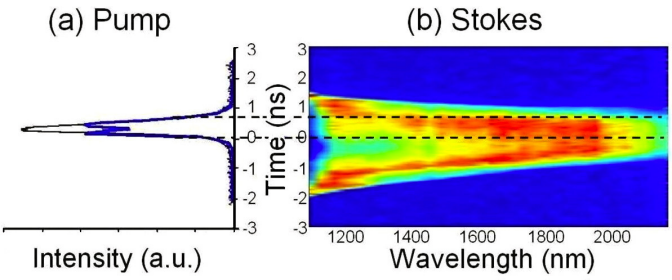

Fig. 9. Superimposition between (a) the distorted (blue) and the gaussian (black) pump pulse, and (b) Stokes wave.

4. Nonlinear saturable transparency

In a second experiment, we recorded the pulse profile at a given wavelength of 1204 nm for several values of the input peak powers. Note that the YDFA is used in this experiment. For a low pump power the converted pulse exhibits a quasi-square shape of 400 ps duration (FWHMI) [see Fig. 10(a)]. As the pump energy increases, the peak power of the converted pulse progressively grows until it saturates. At this stage the maximum peak power is close to 800 W for a pulse duration of 1 ns. Beyond this limit and further increasing the pump, only the energy of the converted pulse increases whereas the peak power saturates. A square pulse envelop of more than 2.6 ns duration with a large central depletion induced by the stimulated Raman scattering is obtained. This saturation is mainly due to the effect of SSFS. Indeed, after the temporal reshaping of the subnanosecond input pulse into several solitonic waves, each soliton is shifted toward another wavelength when exceeding a given intensity threshold. The remaining energy represents the low energy part of the solitonic pulse unaffected by SSFS. This effect of spectral shift obtained above an intensity threshold at a given wavelength, mimics the effect of a saturable transparency and creates a continuum with a limited peak power fixed by the SSFS threshold [see Fig. 10(b)].

Here, the distortion undergone by the input pulse during the continuum generation dramatically changes the overlap between the Stokes and the pump waves. In the time domain, because of the nonlinear conversion obtained down to the pump pulses edges, the obtained infrared pulses are much longer than the original pump pulse. Then, only a small part of the continuum energy is temporally synchronized with the energetic part of the initial pump wave (see Fig. 9). This weak overlapping between stokes and pump waves introduces a limitation of the CARS efficiency. In Fig. 8, the pump was delayed by $\sim$300 ps using the Herriott-type delay line so as to maximize the temporal overlapping and thus CARS efficiency.

An increase of the input pulse power leading to the continuum generation does not overcome this drawback; Indeed, for higher peak power, a broader continuum is obtained with longer wavelengths in the infrared domain while the energy at intermediate wavelengths, located in the central part of the continuum, grows by means of a temporal broadening keeping constant their peak power. Because of the linear dependence of the CARS signal with respect to the Stokes peak power, no improvement of the output signal is obtained by increasing the input pulse peak power at the PCF input.

Finally, to illustrate the applicability of our nanosecond supercontinuum source to multiplex CARS spectroscopy, we have measured the CARS spectra of several samples, namely indene, parafilm and human hair, which are represented in Fig. 11(a), (b) and (c), respectively. It is worth to note that none of the samples was damaged by laser illumination during the experiment.

#178746 - $15.00 USD Received 6 Nov 2012; revised 30 Nov 2012; accepted 30 Nov 2012; published 20 Dec 2012

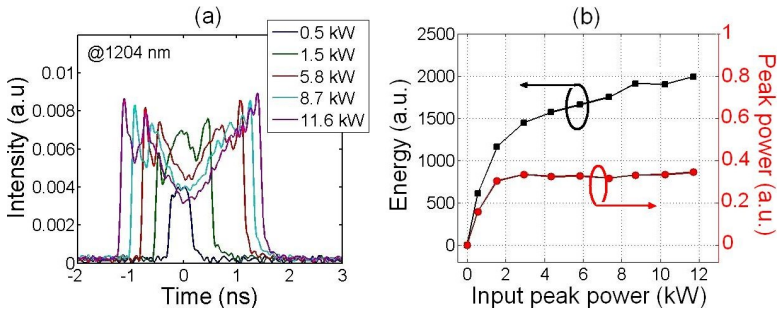

Fig. 10. (a) Evolution of the pulse profile at 1204 nm at the output of the PCF for different input peak power; (b) evolution of the output pulse energy and peak power at 1204 nm vs. peak power at the input of the PCF.

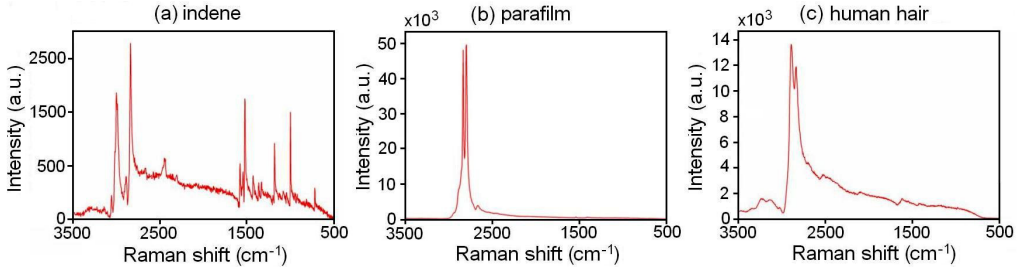

Fig. 11. Multiplex CARS spectra of (a) indene, (b) parafilm, and (c) human hair. These spectra are not intensity-corrected.

5. Conclusion

We have proposed a new compact laser source specifically designed for multiplex-CARS microspectroscopy. This ultrabroadband light source is based on the combination of a subnanosecond microchip laser with a repetition rate of 75 kHz, an YDFA amplifier and an air-silica PCF.

We performed a detailed analysis of the time-frequency distortions undergone by the Stokes wave during nonlinear propagation in fibre amplifier and photonic crystal fibre. We pointed out the impact of Raman effect interplaying with modulation instability and soliton propagation upon the generation of the SC used as Stokes component for multiplex-CARS application. The nonlinear temporal broadening of the Stokes pulse is mainly due to the depletion in the central part of the pulse that undergoes the Raman and solitonic effects. Thanks to both the subnanosecond duration of the pump pulse and the short length of the fiber, a weak impact of dispersion and group-velocity dispersion is observed during propagation in the PCF. However, we demonstrated that the temporal superimposition between the pump and the Stokes beam is dramatically impaired since less than half of the initial energy of the Stokes wave contributes to the CARS process. We emphasize the saturation of the Stokes wave peak power during SC generation because of SSFS. This effect limits the CARS efficiency and cannot be compensated simply by increasing the initial pulse peak power. We also performed chemical and biological studies in order to verify the applicability of this laser source to M-CARS microspectroscopy. The obtained results open the way to the use of sub-nanosecond microchip-based SC sources in the CARS applications, as a promising alternative to narrowband picosecond or transform-limited femtosecond laser sources.

#178746 - $15.00 USD Received 6 Nov 2012; revised 30 Nov 2012; accepted 30 Nov 2012; published 20 Dec 2012